PASJ: Publ. Astron. Soc. Japan **65**, S15, 2013 December 5

A Study of Coronal Holes Observed by SOHO/EIT and the Nobeyama Radioheliograph

Sachiko AKIYAMA,[1,2] Nat GOPALSWAMY,[2] Seiji YASHIRO,[1,2] and Pertti MÄKELÄ[1,2]
[1]*The Catholic University of America, Washington, DC 20064, USA*
[2]*NASA Goddard Space Flight Center, Greenbelt, MD 20771, USA*
sachiko.akiyama@nasa.gov

(Received 2013 July 31; accepted 2013 October 11)

Abstract

Coronal holes (CHs) are areas of reduced emission in EUV and X-ray images that show bright patches of microwave enhancements (MEs) related to magnetic network junctions inside the CHs. A clear correlation between the CH size and the solar wind (SW) speed is well known, but we have less information about the relationship between MEs and other CH and SW properties. We studied the characteristics of 21 equatorial CHs associated with corotating interaction regions (CIRs) during 1996 to 2005. Our CHs were divided into two groups according to the intensity of the associated geomagnetic storms: $Dst \leq -100$ nT (10 events) and > -100 nT (11 events). Using EUV 284 Å images obtained by SOHO/EIT and 17 GHz microwave images obtained by the Nobeyama Radioheliograph (NoRH), we found a linear correlation not only between the maximum SW speed and the area of EUV CH ($r = 0.62$), but also between the maximum SW speed and the area of the ME ($r = 0.79$). We also compared the EUV CH areas with and without an overlapping ME. The area of the CHs with an ME is better correlated with the SW speed ($r = 0.71$) than the area of those without an ME ($r = 0.36$). Therefore, the radio ME may play an important role in understanding the origin of SW.

Key words: Sun: corona — Sun: radio radiation — Sun: solar wind

1. Introduction

Coronal holes (CHs) contain open magnetic fields, and are sources of the high-speed solar wind (SW). Since they have lower densities and temperatures than in quiet-Sun regions, they can be easily identified as areas of reduced emission in EUV and soft X-ray images (Munro & Withbroe 1972; Zirker 1977). Images in the He I 10830 Å absorption line, obtained by ground-based observatories, have also been used to trace CHs (Harvey & Sheeley 1977; Andretta & Jones 1997). The first continuous observations using EUV and X-ray instruments aboard the *Skylab* space station revealed that CHs appear not only in the polar-regions, but also at mid- and low-latitudes (Huber et al. 1974; Zirker 1977). Complex magnetic fields during the solar maximum generate many CHs everywhere on the solar disk, but the polar CHs disappear. As the solar activity decreases, the polar CHs reappear and expand toward the equator. During the declining phase of the solar cycle, extended polar CHs or isolated CHs are often observed around mid- and low-latitudes (Waldmeier 1981; Fox et al. 1998).

Microwave enhancements (MEs) observed in a narrow range of wavelengths are also known to be present inside CHs (Kundu & McCullough 1972; Kosugi et al. 1986; Gopalswamy et al. 1998, 1999, 2000; Moran et al. 2001). According to Gopalswamy et al. (1999), MEs have a close relationship to the enhanced unipolar magnetic regions within CHs. Moreover, the locations of MEs coincide temporally and spatially with magnetic network junctions inside the CHs at the chromospheric level. Moran et al. (2001) reported that the signatures of bright patches inside MEs coincide with the Hα bright spots caused by bright fibrils and a lack of dark fibrils. They also pointed out that some radio and EUV bright points occur from different physical layers of the concentrated magnetic flux area because of a co-spatial enhancement between radio and Fe XII EUV emissions, which are the bases of coronal plumes. In many cases MEs are small and localized compared to the signatures in the EUV, X-ray, and He I 10830 Å images. The average ME area occupies only 33% of the area, seen in EUV CH (Gopalswamy et al. 2000).

Low-latitude CHs are especially of interest from the view point of space weather in the ecliptic plane. High-speed SW from low-latitude CHs are known to produce corotating interaction regions (CIRs) that cause geomagnetic storms (Krieger et al. 1973; Gosling 1996; Balogh et al. 1999; Tsurutani et al. 2006, and references therein). When the high-speed (700–800 km s^{-1}) streams from CHs interact with the low-speed (300–400 km s^{-1}) streams ahead of them, both the magnetic field and the plasma are compressed at the boundary. This increase in the magnetic field strength results in geomagnetic storms lasting for several days (Burlaga & Lepping 1977; Tsurutani & Gonzalez 1987). Hence, the ability to predict the speed of the SW streams emanating from low-latitude CHs is especially valuable for space weather forecasting. Nolte et al. (1976) found a linear correlation between the area of the low-latitude CHs and the SW speed, except for small or very large CHs. This characteristic was interpreted as being an effect of the expansion of magnetic flux tubes (Levine et al. 1977), and was demonstrated using the potential-field source surface model (Wang & Sheeley 1990). Ohmi et al. (2004) also reported slow ($V < 350$ km s^{-1}) SW from low-latitude CHs located in the vicinity of the active region (AR), and pointed out the effect of the surrounding magnetic field structures

on the speed of SW from CHs. Fisk, Schwadron, and Zurbuchen (1999) suggested that the magnetic field strength is one of the coronal properties related to the SW speed. Fujiki et al. (2005) reported that the solar wind speed during the solar minimum is related to the product of the inverse expansion rate and the photospheric magnetic field strength.

Coronal mass ejections (CMEs) generally cause severe geomagnetic storms (see e.g., Gopalswamy et al. 2007). Only $\sim 10\%$ of large geomagnetic storms ($Dst \leq -100$ nT) are caused by CIRs (Richardson et al. 2006; Zhang et al. 2007; Gopalswamy 2008), and the intensities of the CIR-caused storms are much weaker than those associated with interplanetary CMEs. The CIR storms predominantly occur during the declining phase to the minimum phase of the solar cycle (Tsurutani et al. 2006). Considering the space weather aspect, Vršnak, Temmer, and Veronig (2007a, 2007b) showed a clear correlation between the daily average area of CHs near the disk center and the daily average SW properties during the solar minimum. They also demonstrated the temporal sequences of the daily average SW parameters in CIRs. Gopalswamy (2008) identified the source region of a large geomagnetic storm as being a large disk-center CH in soft X-rays that showed an enhanced magnetic field and ME.

In this paper, we compare the observations of low-latitude EUV CHs and MEs associated with intense and weak geomagnetic storms caused by CIRs, and relate those observations to the SW properties observed at 1 AU. In section 2, we describe the data selection for CHs associated with 10 large and 11 weak geomagnetic storms, and how the EUV CHs and MEs are measured. In section 3, we show the relationship of the maximum SW speed with the properties of the EUV CH and ME. Finally, we discuss the use of the magnetic flux tube expansion rate, f, the photospheric absolute magnetic field strength, $B_{\rm CH}$, and the combination of $B_{\rm CH}/f$ in modeling and predicting the SW speed.

2. Observations

2.1. Data Sets

Since CHs close to the disk center are more geoeffective (Nolte et al. 1976), we investigated the existence of a low-latitude CH on the solar disk starting from 5 d before the time of the minimum *Dst* associated with CIRs. The disturbance storm-time index, *Dst*, which is a measure of the strength of the ring current, is used as a reference index of geomagnetic activity. Hourly *Dst* data are provided by the World Data Center for geomagnetism of Kyoto University.[1] Our low-latitude CHs are divided into two groups based on the intensity of the associated geomagnetic storm. The first group is a set of 10 CHs associated with a large storm (minimum $Dst \leq -100$ nT) (Richardson et al. 2006; Zhang et al. 2007). These 10 large storms were among the 88 major storms during solar cycle 23 (1996–2005) investigated extensively at the Coordinated Data-Analysis Workshop (CDAW)[2] held in 2005 and 2007. The other group has 11 low-latitude CHs associated with a weak storm (minimum $Dst > -100$ nT) during the solar minimum in 1996. The CIRs originating from these CHs were among the 37 stream interaction regions (SIR) listed by Jian et al. (2006).

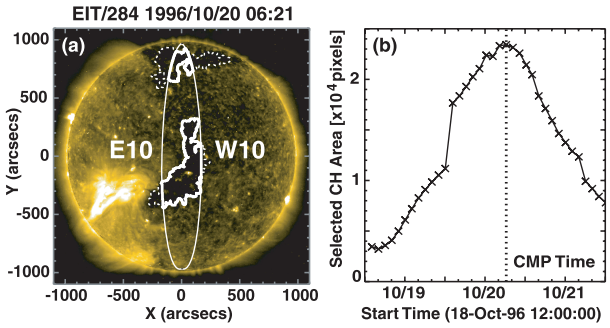

Fig. 1. (a) Coronal hole (CH), as observed in the SOHO EIT 284 Å image on 1996 October 20. The dark areas enclosed by the dotted line have a lower intensity than the intensity threshold and hence determine the CH boundary. The central CH area marked by a thick solid line is used to compute the CH central meridian passage (CMP) time. (b) Time profile of the CH area enclosed within the oval marked by the white thin line in figure 1a. The time of maximum CH area is defined as the CMP time.

Figure 1a shows a EUV 284 Å image obtained by the Extreme-ultraviolet Imaging Telescope (EIT) on board SOHO with the area of intensity being less than our CH threshold (see below), marked by the doted line. Since the EUV intensity in low-latitude CHs varies by a factor of about 3 between the solar maximum and minimum (Harvey et al. 1982; Belenko 2001), a fixed intensity threshold cannot properly determine the CH boundaries for all phases of the solar cycle. Therefore, EIT CHs are described as areas having the EUV intensity below the threshold defined as half of the median EUV intensity of the whole solar disk. The thick solid line marks the low-latitude CH area assumed to be the source of the Earth-directed high-speed SW. To make a simple comparison between the CH area and the SW speed, we selected the CH area within 10° in longitude from the central meridian (CM) and 30° in latitude from the disk center. Figure 1b shows a time profile of the CH area starting from 5 d before 1996 October 23, when the minimum *Dst* recorded was −105 nT. Each data point was derived from aligned EIT 284 Å images separated at least by a two-hour interval. We consider this to be a continual area variation of the real low-latitude CH. The time of the maximum area is the CM passage (CMP) time of the CH. Twelve out of the 37 SIR events in 1996 are associated with low-latitude CHs.

2.2. Solar Data

We used three different data sets to obtain CH properties: (1) coronal EUV 284 Å images obtained by EIT, (2) 17 GHz microwave images acquired by the Nobeyama Radioheliograph (NoRH), and (3) photospheric magnetograms obtained by the Michelson Doppler imager (MDI) on board SOHO. Figure 2 shows an example of a low-latitude CH as visible in (a) magnetogram, (b) EUV, and (c) 17 GHz microwave images. All data are aligned to the CMP time (1996 October 20 06:21 UT) of the CH.

Figure 2a shows an average magnetic field map calculated from the three sequential MDI images displayed with a scaling

[1] ⟨http://wdc.kugi.kyoto-u.ac.jp/dstdir/⟩.
[2] ⟨http://cdaw.gsfc.nasa.gov/meetings/2005_gmstorm/⟩.

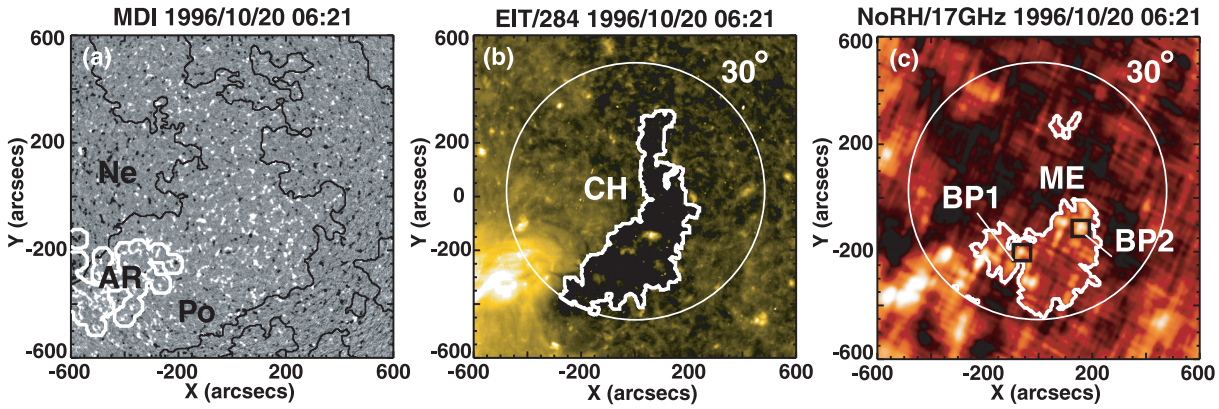

Fig. 2. CH on 1996 October 20 as seen in (a) the magnetogram (SOHO/MDI), (b) the 284 Å (SOHO/EIT) image, and (c) the 17 GHz microwave image (NoRH). The microwave image was enhanced by a histogram-equalizer method using the IDL program "hist_equal.pro" to see details of the microwave enhancements (MEs). The active region boundaries and the large-scale magnetic inversion lines are denoted by white and black lines, respectively in panel (a). The CH boundaries in EUV (b) and radio (c) within the 30° zone from the disk center are outlined in white thick solid lines. Two microwave bright points are marked by black squares as BP1 and BP2.

of −30 G to +30 G. We ignore the small-scale structures and evolutions, because the location of both the CH and the ME relates to the enhanced large-scale unipolar magnetic field regions (Gopalswamy et al. 1999). The black thin lines mark the border between the large-scale positive (Po) and negative (Ne) magnetic field areas in a smoothed image where any given pixel gives the median field strength within the area covering 20 pixels (≈ 30000 km) in the vertical and horizontal directions. We also get the CH main polarity from the smoothed large-scale magnetic field map. The method used to obtain the large–scale magnetic field image is also described in Gopalswamy et al. (2009).

Figure 2b shows an EUV image with a low-latitude CH within 30° from the disk center, indicated by the white thick line. The CH boundary is marked by the contour at half the median intensity of the solar disk. The range of the intensity threshold varied from 1.09 data number (DN) to 5.37 DN in this study. The white thick line in figure 2b corresponds the contour at 1.21 DN level. Although CHs are thought to have unipolar magnetic fields, in some cases the CH areas as defined above include large-scale opposite polarity regions. In those cases, we excluded the opposite polarity areas from the defined CH areas. We also eliminated possible filaments located at the CH edge from the final area.

Figure 2c shows a histogram-equalized microwave image made by averaging five 17 GHz microwave images taken at 10-minute intervals. We can see MEs as brighter, broadened areas of enhanced emission enclosed by a white thick line. The MEs are defined as areas that are brighter than three-quarters of the median radio intensity of the solar disk. Since both the ME and the AR are identified as bright regions in microwave images (Kosugi et al. 1986; Gopalswamy et al. 1999), we used magnetic field data to exclude ARs. The ME area located within 20 pixels from strong magnetic field of ARs, were treated as being due to ARs. We could not use the fixed threshold to define the strong magnetic field area because of the solar cycle variation. In each magnetogram, the threshold ($B_{\rm th}$) is defined as $B_{\rm th} = B_{\rm m} + \sigma B$, where $B_{\rm m}$ and

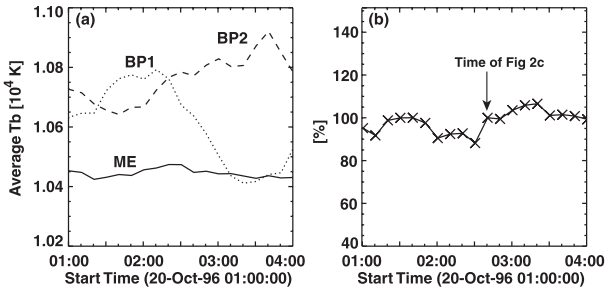

Fig. 3. (a) Time profiles of the brightness temperature variation of ME and the two microwave bright points marked in figure 2c. (b) Time profile of the ratio of MEs area based on the MEs outlined by the white thick lines in figure 2c. The observational time of figure 2c is marked by the arrow.

σB are the median and the standard deviation of the unsigned magnetic field strength of the solar disk, respectively. We show the AR enclosed by the white line by letter "AR" in figure 2a. In the case of figure 2a, the threshold is 126 G. The thresholds range from 66 G (solar minimum) to 344 G (solar maximum). We also excluded the minor polarity area from the selected ME area.

There are small bright points (BPs) in the MEs (see figure 2c). The BPs are located above the magnetic elements in the magnetogram, and the brightness of the BPs changes over a timescale of 0.5–3 hr (Gopalswamy et al. 1999). One might think that the changes of the BPs affect the ME parameters used in this paper, but that is not the case. Two dashed lines in figure 3a show the brightness of two BPs as a function of time. The BP brightness changed in a few hours, but the average brightness of the ME (solid line) remained constant. Figure 3b shows that the selected ME area varies within 10% in 4 hr. Therefore, the ME area and average brightness are adequate parameters to compare to the solar wind parameters near the Earth.

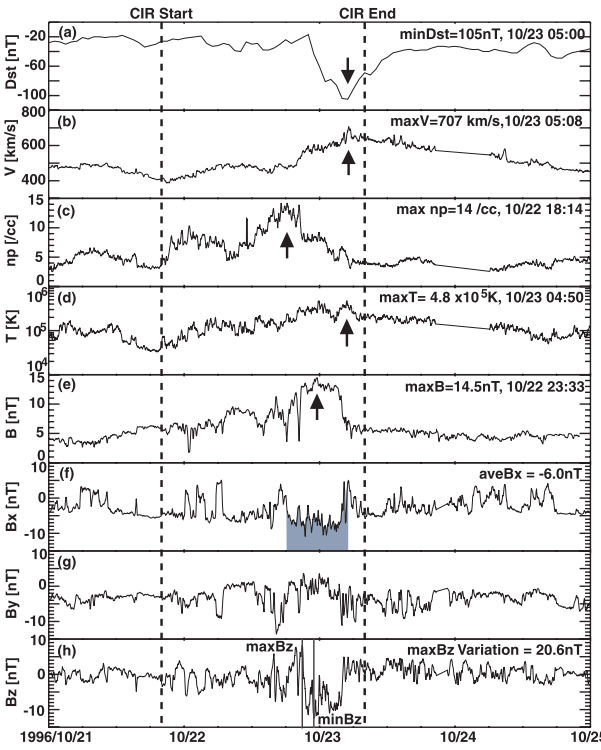

Fig. 4. High-speed stream and geomagnetic activity from 1996 October 21 to October 25. Top panel (a) is the *Dst* index. Panels (b)–(d) are velocity, density, and temperature of the solar wind (SW) respectively (SWE/WIND). Panels (e)–(h) are total magnetic field, and x, y, and z components of magnetic field (MFI/WIND) in Geocentric Solar Magnetospheric (GSM) cordinates. The start and end times of the CIR and the extreme values (indicated by arrows) are shown in each panel. The period used to calculate the average x component of the magnetic field is shown as a gray area in panel (f). The times of the maximum and minimum z component of the magnetic field during the CIR are marked by the thin solid lines in panel (h).

2.3. *Interplanetary Data*

We examined the properties of CIRs using the Solar Wind Electron, Proton, and Alpha Monitor (SWEPAM) and the magnetometer instrument (MAG) on board the Advanced Composition Explorer (ACE) spacecraft. For the storm in 1996, we used data from the Solar Wind Experiment (SWE) and the Magnetic Field Investigation (MFI) on board the Wind spacecraft. Since both spacecraft are located in the interplanetary medium, there is about a 1 hr delay for the transit of SW structures from the spacecraft to Earth. The time resolution of the ACE and Wind data are 64 s and 92 s, respectively. We obtained the data from the NASA Coordinate Data Analysis Web,[3] and used the proton speed (V), proton density (n), proton temperature (T), total magnetic field magnitude (Bt_IP), x, y, and z components of magnetic field (B_x_IP, B_y_IP, and B_z_IP) averaged over a ten-minute time window.

Figure 4 shows SW parameters of the CIR-induced magnetic storm on 1996 October 23 as an example. The top panel (figure 4a) shows the *Dst* index. The next seven panels (figures 4b–4h) are the SW proton speed, proton density, proton temperature, total interplanetary magnetic field, and x, y, and z components of the magnetic field obtained by Wind in Geocentric Solar Magnetospheric (GSM) cordinates. The dashed lines stand for the CIR start and end times. The extreme values of each parameter are marked with arrows in figures 4a–4e. The average value of the magnetic field x component was calculated over the time period shown as the gray filled region in figure 4f. This gray filled region marks the interval from the peak density considered to be the boundary between the slow and fast SW streams to the peak velocity. We mark the maximum and minimum of the magnetic field z component by the solid lines in figure 4h. The maximum variation computed from the maximum and minimum values of B_z_IP is also noted in figure 4h.

2.4. *Events*

In order to check our CH and geomagnetic storm associations, we examined the x component of the interplanetary magnetic field (B_x_IP) of the CIRs and the line-of-sight magnetic field of the source CHs, and confirmed that in all the events they have a consistent polarity. For the event on 2002 October 14, there were three candidate CHs on 2002 October 11: one on the equator and the other two on the northern and southern hemispheres. Richardson et al. (2006) and Zhang et al. (2007) selected the CH on the northern and the southern hemisphere, respectively. The southern CH had a predominantly positive polarity, i.e., the magnetic field was pointing away from the Sun. However, the B_x_IP of the CIR and the high-speed stream were both positive, meaning that the field lines were pointed towards the Sun. Therefore, based on the polarity consistency, we think that there are two likely candidates (the northern and the equatorial CH). Considering the Sun-Earth connection, the equatorial CH seems to be the better candidate. However, the high-speed stream had a long duration (more than 100 hr), which is consistent with the large CH on the north, rather than the small equatorial CH. Hence, we selected the northern CH as the source of the CIR.

Tables 1 and 2 summarize the 10 large and 11 weak CIR-generated geomagnetic storms together with the CH properties at the Sun and SW properties at 1 AU, respectively. In columns 1 and 2, we have listed the start time of the geomagnetic storm and the minimum value of the *Dst* index. Columns 3, 4, and 5 are the CH CMP time, the central latitude of the CH, and the main polarity of the CH. Column 6 gives the intensity threshold of the EUV CH in units of image DN. We have listed the CH area, the average CH intensity, and the average absolute magnetic field strength within 30° from the disk center in columns 7, 8, and 9, respectively. Column 10 gives the brightness temperature threshold of the ME in units of K. Columns 11, 12, and 13 list areas of the ME, the average brightness temperature, and the average absolute magnetic field strength, respectively. We also note the CIR start and end time in columns 13 and 14. The maximum speed, V (column 15), and the maximum density, n (column 16), are listed with observation times in parentheses. Column 17 is the average B_x_IP during the period between the maximum density and the maximum speed. In the last column 18, we note the variance of B_z_IP, calculated from the absolute minimum and maximum B_z_IP.

[3] ⟨http://cdaweb.gsfc.nasa.gov/istp_public/⟩.

Table 1. Intence storms.

GM Storm		EIT							Radio				Interplanetary							
Time	*Dst* [nT]	CMP time	Lat	P*	$I_{\rm th}$† [DN]	Area [10^{10} km^2]	I [DN]	$\lvert B\rvert$ [G]	$TB_{\rm th}$‡ [K]	Area [10^{10} km^2]	Tb [K]	$\lvert B\rvert$ [G]	CIR Start	CIR End	Max V (time) [km s^{-1}]		Max N (time) [cm^{-3}]	$\overline{B_x}$ [nT]	Var B_z§ [nT]
96/10/23 05	−105	96/10/20 06:21	S10	+	1.21	7.87	1.29	7.3	10136	5.74	10448	8.9	10/21 20	10/23 08	707	(10/23 05:08)	14.2 (10/22 18:14)	−6.0	20.6
98/03/10 21	−116	98/03/08 09:03	S30	−	1.40	2.13	1.25	7.1	10339	2.09	10476	8.3	03/09 21	03/11 04	567	(03/11 02:57)	53.4 (03/10 09:36)	6.0	31.7
02/09/04 06	−109	02/08/31 17:06	S15	+	3.92	5.70	3.84	14.8	10324	3.25	10760	18.7	09/03 02	09/04 19	476	(09/04 11:49)	38.2 (09/03 18:49)	−3.2	34.1
02/10/07 08	−115	02/10/05 09:06	S07	+	4.79	9.60	3.00	11.2	10382	1.37	10653	15.7	10/07 00	10/08 06	525	(10/08 02:06)	16.1 (10/07 01:30)	−5.9	21.0
02/10/14 14	−100	02/10/12 09:06	N00	−	4.93	2.65	4.29	13.7	10365	0.91	10516	24.2	10/14 02	10/16 04	607	(10/16 01:54)	40.1 (10/14 10:51)	5.2	29.2
02/11/21 11	−128	02/11/18 13:21	S04	+	5.32	8.84	3.52	12.5	10169	7.82	10528	14.4	11/20 10	11/21 13	752	(11/21 12:07)	81.0 (11/21 02:03)	−4.0	51.3
03/07/12 06	−105	03/07/08 13:26	N04	−	3.78	7.31	2.66	13.3	10211	6.27	10616	14.1	07/11 00	07/12 20	739	(07/12 17:41)	25.3 (07/11 16:05)	6.2	26.2
04/02/11 18	−109	04/02/10 15:06	N02	−	1.95	15.47	1.65	10.0	10296	8.64	10581	11.0	02/11 01	02/12 14	723	(02/11 06:34)	17.1 (02/11 18:45)	9.9	23.2
05/05/08 14	−127	05/05/06 15:03	N10	−	2.22	8.30	1.46	10.6	10006	5.20	10515	11.8	05/07 18	05/10 08	882‖	(05/08 12:29)	60.5 (05/07 20:42)	4.9	29.3
05/08/31 16	−131	05/08/28 15:06	S12	+	2.25	3.84	1.96	13.8	10329	2.20	10665	16.4	08/30 18	09/01 04	502	(09/01 03:59)	40.3 (08/31 12:15)	−3.3	35.0

* Main polarity of CHs.
† Intensity threshold of EIT CHs.
‡ Brightness Temperature threshold of radio enhancements from nomal radio images.
§ Maximum variation computed from the maximum and minimum values of B_z_IP.
‖ Possibility of a contamination of coronal mass ejection.

Table 2. Weak storms.

GM Storm		EIT							Radio				Interplanetary							
Time	*Dst* [nT]	CMP time	Lat	P	$I_{\rm th}$ [DN]	Area [10^{10} km^2]	I [DN]	$\lvert B\rvert$ [G]	$TB_{\rm th}$ [K]	Area [10^{10} km^2]	Tb [K]	$\lvert B\rvert$ [G]	CIR Start	CIR End	Max V (time) [km s^{-1}]		Max N (time) [cm^{-3}]	$\overline{B_x}$ [nT]	Var B_z [nT]
96/01/20 07	−37	96/01/17 16:36	N15	+	0.51	3.77	0.48	4.2	10270	1.77	10426	6.6	01/19 14	01/21 02	532	(01/20 04:37)	21.6 (01/19 22:28)	−3.7	17.3
96/08/09 23	−9	96/08/04 07:36	S30	−	1.93	0.09	1.91	9.8	10339	0.01	10371	10.5	08/08 00	08/10 12	415	(08/09 13:06)	12.7 (08/09 01:06)	2.8	14.2
96/08/29 06	−48	96/08/26 17:05	N00	+	1.51	5.48	1.32	10.0	10180	4.87	10473	12.6	08/28 15	08/29 15	628	(08/29 14:49)	21.3 (08/29 00:34)	−2.2	15.2
96/09/05 00	−30	96/08/31 18:52	N00	−	1.76	1.50	1.72	9.2	10272	0.11	10323	8.6	09/03 18	09/07 00	456	(09/06 08:28)	24.0 (09/04 09:18)	9.1	15.7
96/09/27 01	−50	96/09/23 01:44	N24	+	1.42	3.77	1.25	9.5	10192	4.93	10476	11.9	09/26 14	09/26 22	684	(09/26 21:24)	30.5 (09/26 17:25)	−0.4	34.2
96/10/02 08	−15	96/09/27 10:06	N05	−	1.52	6.65	1.37	14.4	10307	0.61	10439	15.3	10/01 18	10/03 00	561	(10/02 23:30)	41.5 (10/02 02:53)	4.0	22.8
96/10/28 09	−20	96/10/24 12:06	N00	−	1.51	7.14	1.39	8.0	10252	2.02	10699	14.1	10/27 20	10/28 12	621	(10/28 11:53)	17.8 (10/27 23:38)	5.5	16.0
96/11/14 12	−47	96/11/09 13:40	S08	+	1.07	2.57	1.04	5.0	10306	0.90	10412	6.1	11/13 13	11/14 12	504	(11/14 09:10)	42.4 (11/13 17:30)	−0.2	24.1
96/11/25 06	−28	96/11/21 16:36	S20	−	1.58	2.25	1.47	10.1	10280	1.51	10428	11.3	11/24 00	11/25 06	481	(11/24 23:05)	34.8 (11/24 08:44)	2.9	16.5
96/12/10 01	−32	96/12/07 04:06	N35	+	1.19	1.69	1.18	5.0	—	—	—	—	12/09 16	12/10 12	553	(12/10 11:32)	44.6 (12/09 21:44)	−4.6	22.3
96/12/14 21	−25	96/12/12 06:06	N05	+	1.32	1.25	1.28	6.6	19313	0.60	10589	11.7	12/14 08	12/16 16	579	(12/15 18:56)	10.2 (12/15 02:14)	−4.4	13.1

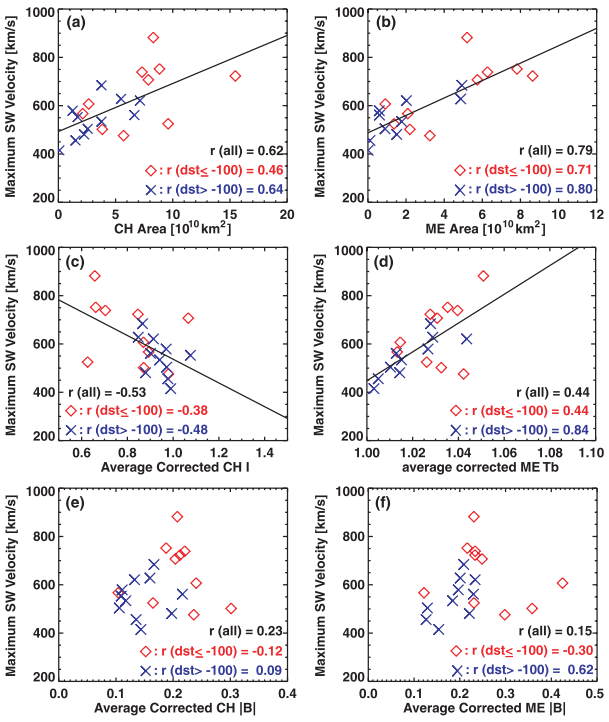

Fig. 5. Scatter plots of the maximum SW speed against the EUV CH (left panels) and ME (right panels) properties, respectively. The diamond and cross symbols stand for the intense and weak storms. The solar properties plotted in the top (a, b), middle (c, d), and bottom (e, f) panels are the area, intensity (or brightness temperature), and magnetic field strength within 30° zones from disk center. The correlation coefficient (r) is noted in each plot.

3. Relation between CH and CIR Properties

3.1. *Comparing CH and ME Parameters*

The linear correlation between the CH area from the soft X-ray images and the maximum SW speed associated with the CIRs is well known (Nolte et al. 1976). Multi-wavelength observations report the shape similarity of large CHs between coronal and He I 10830 Å observations (Harvey & Sheeley 1977; Kahler et al. 1983; de Toma & Arge 2005). In contrast, the ME has a different shape compared to the shape at other wavelengths. For the CH brightness and the magnetic field strength, the relationships with the high-speed SW are not revealed, as compared with that of the CH area, because of the variation in the solar cycle activity. Recently, Luo et al. (2008) and Obridko et al. (2009) reported an inverse relationship between the SW speed and the CH brightness observed at the EUV 284 Å wavelength. With respect to the magnetic field strength, Fisk, Schwadron, and Zurbuchen (1999) also suggested a relationship between the photospheric magnetic field strength and the SW speed from the point of view of the energy transport in CHs.

Figures 5a–5f show scatter plots of the maximum SW speed vs. the CH and ME areas (upper), their intensities (middle), and their magnetic field strengths (bottom). The CH and ME parameters obtained from EIT and radio images are shown in the left and right side panels, respectively. The cross and the diamond symbols stand for the weak (minimum $Dst > -100$ nT) and intense (minimum $Dst \leq -100$ nT) storms, respectively. The correlation coefficient (r) is shown in each panel. In spite of the differences in the details between CH and ME, figures 5a and 5b confirm a good correlation between the area and the SW speed not only for the EUV CHs, but also for the MEs. The correlation coefficient in the case ME ($r = 0.79$) is much higher than that of EUV CH ($r = 0.62$).

Figures 5c and 5d show the relationship of the maximum SW speed with the corrected average EUV CH brightness, and the corrected average ME brightness temperature, respectively. In order to correct the effects of the solar cycle intensity variation, the corrections for the CH brightness and the ME brightness temperatures were made by dividing the average brightness by the threshold, which determines their boundaries. We can see a good correlation with the correlation coefficient of $r = -0.53$ in figure 5c, as was the case with Luo et al. (2008). For the ME brightness temperature in figure 5d, we find a weaker correlation ($r = 0.44$) with the SW speed. It is interesting that the CHs and MEs associated with the high-speed SW appear to be much darker, as observed by EIT, and much brighter, as observed by radio instruments, respectively.

We also show scatter plots between the corrected average absolute magnetic field strength and the maximum SW speed for the CHs and the MEs. The correction was computed by dividing the CH and ME average absolute magnetic field strength by the absolute magnetic field strength of the whole solar disk, excluding ARs. Though both the CHs and the MEs associated with large storms have a tendency to have a higher magnetic field strength, there are no clear correlations visible in figures 5e and 5f. Gopalswamy, Shibasaki, and Salem (2000) performed a large statistical study with radio enhancements using 71 EUV CHs from 1996 January to 1999 April. Their results show a weak correlation between the peak brightness temperature and the peak magnetic field strength within CHs. If the ME area account for a substantial fraction of the CH area, their result is reasonable because of a spatial correspondence between the MEs and the enhanced unipolar magnetic regions. In our case only the weak storm data set in figure 5f show a good correlation ($r = 0.62$). It is interesting to note that in figures 5a–5f the correlation coefficients for the weak storms are bigger than those for the intense storms.

3.2. *Overlapping Area between CH and ME*

The shape of ME is much different from that of EUV and other wavelength CHs, which indicate the boundary of the open magnetic field lines. Therefore, we consider the ME area overlapping with the EUV CH. Figures 6a and 6b show scatter plots of the maximum SW speed as a function of the CH area with and without ME area overlap. The implication of all symbols is identical to that in figure 5; 1996 August 4 and December 7 events have no overlapped CH area with the ME area. We can clearly see a strong correlation ($r = 0.71$) between the CH area with ME overlap and the SW speed. Obviously, the larger is the overlap between the CH and ME areas, the better is the correlation with the SW speed compared to the whole EUV CH area shown in figure 5a. This indicates that the size of the ME area within the EUV CH area can be used as an indicator for intense geomagnetic storms caused by CIRs. The ME signatures correspond to the chromospheric brightness inside CHs

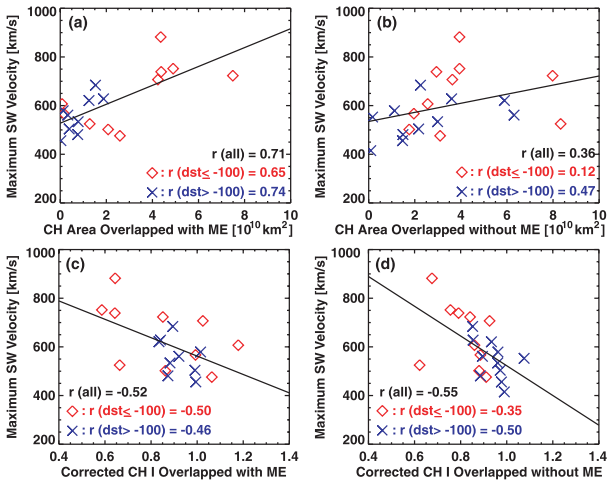

Fig. 6. Scatter plots of the maximum SW speeds against the EUV CH area overlapped with (left panels) and without (right panels) ME properties, respectively. The upper (a, b) and lower (c, d) panels represent the area and intensity. The implication of all symbols is identical to that in figure 5.

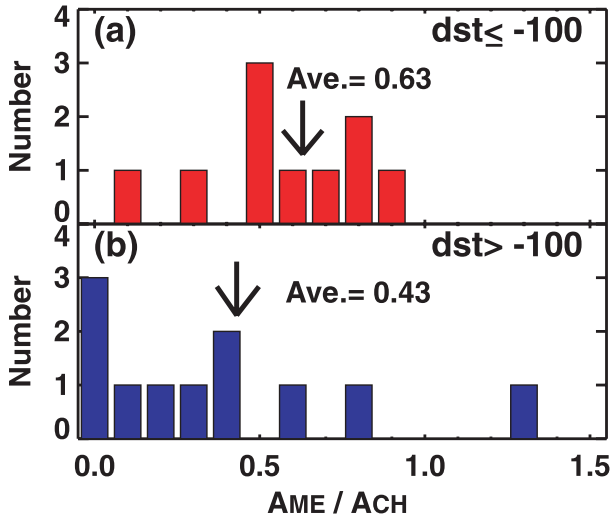

Fig. 7. Histograms of the ME area to EUV CH area ratio for (a) intense and (b) weak geomagnetic storms. Average ratios are marked by the arrows.

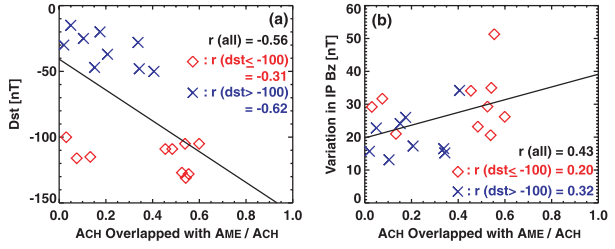

Fig. 8. Scatter plot of the ratio of the CH area overlapped with ME area to the whole CH area with (a) minimum *Dst* index and (b) the variation of the z component of interplanetary magnetic field.

(Gopalswamy et al. 1999; Moran et al. 2001), and hence we have established a connection between the interplanetary SW and the solar chromospheric layer.

We also show scatter plots of the maximum SW speed as a function of the overlapped CH area with and without the ME area for the corrected EUV CH intensity (figures 6c and 6d). Figures 6c and 6d show inverse relationships to the EUV intensity with a similar correlation coefficient as in figure 5c. Little difference between the area with and without an ME overlap means that the EUV intensity does not show much spatial difference inside CH.

3.3. Intense and Weak Geomagnetic Storms

Our CH data set consists of the source regions of CIRs associated with the intense and weak geomagnetic storms. In this section we discuss the relationship between the EUV CHs, while taking into the consideration the MEs and the geomagnetic storms. Figures 7a and 7b plot histograms of the ratio of the ME area relative to the EUV CH area in events associated with intense and weak storms, respectively. The average ratios of the ME area to the EUV CH area are 0.55 (all data set), 0.63 (intense storms), and 0.43 (weak storms). Figures 7a and 7b indicate that CHs, which have a large ME area to the EUV CH area ratio, tend to produce intense geomagnetic storms. Gopalswamy, Shibasaki, and Salem (2000) examined the ratio of the ME area relative to the CH area observed by EIT 284 Å for the period from 1996 January to 1999 April, and found that the average ratio is 0.33. Our results give a larger ratio than that of Gopalswamy, Shibasaki, and Salem (2000). This difference may come from the difference in the analyzed time period. There was only one large geomagnetic storm during the period studied by Gopalswamy, Shibasaki, and Salem (2000). Additionally, since the number of large CHs decreases with the increasing solar activity, our data may have a higher proportion of large CHs because our study period corresponds to the minimum phase. One more point of focus in figure 7 is that the area ratios are dispersed from 0.07 to 1.31 for the weak storms (in figure 7b). We checked the two events with a particularly-high ratio (1996 August 26 and September 23) in figure 7b, and found that both events are associated with the famous trans-equatorial CH known as the "elephant trunk" CH (Gopalswamy et al. 1999; Del Zanna & Bromage 1999; Gibson et al. 1999). The "elephant trunk" CH, which appeared at the end of 1996 August, extended from the northern polar CH to the southern hemisphere as a slender "elephant trunk" feature, and lived on for about three months. Actually, the SW speeds of both "elephant trunk" CHs (628 km s^{-1} and 684 km s^{-1}) are the two fastest speeds in the weak storm data set. Therefore, the two events with the high ratio in figure 7b may have peculiar characteristics. The wide-ranging dispersion means that other factors may also influence the *Dst* index and the interplanetary SW speed (see section 4).

Figures 7a and 7b indicate that the ME area to EUV CH area ratio relates to the intensity of the geomagnetic storm. Moreover, figure 6a shows that the EUV CH area overlapped with ME area may be more closely associated with the high-speed SW than the whole CH area. Therefore, we show a scatter plot of the minimum *Dst* index with the ratio of the EUV CH area overlapped by ME area ($A_{\mathrm{CH\_OME}}$) relative to

the EUV CH area ($A_{\rm CH}$) in figure 8a. The implication of all symbols is identical to that in figure 5. Figure 8a shows a negative correlation with the correlation coefficient of $r = -0.56$. Verbanac et al. (2011) computed the fraction of the CH area in the central meridian slice $\pm 10^\circ$ from 2005 January 25 to May 5, and showed a correlation plot between the fraction of the CH area and the minimum *Dst* associated with each CH. Their plot revealed a large scatter with a correlation coefficient of $r = -0.27$. Moreover, what is noticeable in figure 8a is that the three diamond points (1998 March 8, 2002 October 5, and 2002 October 12) of the large storm data set correspond to a small $A_{\rm CH\_OME}$-to-$A_{\rm CH}$ ratio. If these three points are left out of consideration, the correlation coefficient in figure 8a becomes much better ($r = -0.89$). According to Richardson et al. (2006), the large geomagnetic storms ($Dst \leq -100$ nT) generated by CIRs during the solar cycle 23 exhibit periods of a southward-pointing magnetic field caused by the compressed plasma around the following locations: (1) from the stream interface to the CIR trailing edge, (2) at the region significantly preceding the stream interface, and (3) at both before and after the stream interface. Two of the small-ratio events associated with the large storms occurred in 2002 October, and the lowest recorded *Dst* index was less than -30 nT before the CIR arrival because of intense preconditioning activity. Hence, we suppose that these large geomagnetic storms might have occurred under influences other than the area ratio of $A_{\rm CH\_OME}$ to $A_{\rm CH}$.

Richardson et al. (2006) also note that the large storms are often observed in CIRs having a large variation of B_z_IP, i.e., with not only the southward pointing, but also the northward pointing of the B_z component. The Alfven waves moving out from the Sun affect the B_z component of the magnetic field (Belcher & Davis 1971), and are considered to be amplified with their propagation (Tsurutani et al. 1995). In order to investigate whether the variation of B_z_IP is one of the other factors that cause large storms, even if the $A_{\rm CH\_OME}$ to $A_{\rm CH}$ ratio is small, we show the relationship between the CH area ratio and the variation of the B_z component of the magnetic field in figure 8b. The variation of B_z_IP is calculated by adding the absolute the minimum and maximum B_z components during the period from the CIR start to the end. Figure 8b shows a weak positive association, and indicates a low probability of the variation of B_z_IP being the other factor.

4. Discussion

4.1. Geomagnetic Storm on 2005 May 8

The highest fast wind speed in our data set is 882 km s^{-1}, which exceeds the typical speed range of the fast SW (700–800 km s^{-1}). The event is the intense magnetic storm ($Dst = -127$ nT) on 2005 May 8. Zhang et al. (2007) identified that the storm was caused by a CIR solely. However, Chertok et al. (2013) suggested that the storm was possibly caused by a fast halo CME (speed = 1128 km s^{-1}: Yashiro et al. 2004) associated with C8.5 flare (S08E28) on 2005 May 6 at 16:03 UT. If we exclude this event from the analysis, almost all correlation coefficients (r) derived in the paper remain the same, or improved. For example, the correlation between the SW speeds and the EUV CH areas changed from 0.62 to 0.63 (figure 5a). The correlation between the SW speeds and the ME areas improves from 0.79 to 0.84 (figure 5b). Therefore, the MEs have strong connections to the SW.

4.2. Microwave Enhancements and Fast Solar Wind

We show in figure 6 that the SW speed shows better correlation with the area of the CHs with an ME ($r = 0.71$) than the area of those without an ME ($r = 0.36$). Therefore, the MEs should have important information about the SW acceleration mechanism. However, it is still unknown why parts of CHs are bright in the microwave region, so the connection between the MEs and fast SW is also unclear. Here, we discuss two possibilities.

One possibility is that the ME is an indicator of energy input at the bottom of the open flux tube. Gopalswamy et al. (1998, 1999) confirmed that the contribution from the coronal plasma is negligible, and concluded that the MEs originate from plasma at the chromospheric temperature. They also pointed out that MEs are possibly due to network microflares at the bottom of the CHs, as originally proposed by Parker (1991). In the Parker's model, 80% of released energy dissipates quickly at the coronal base, and the remaining 20% transforms to the Alfven wave, which dissipates at 5–20 $R_{\rm S}$. The former and the latter are responsible for the MEs and the SW acceleration, respectively.

The other possibility is that the ME is an indicator of the expansion factor of the open flux tube. Wang and Sheeley (1990) obtained an empirical relationship between the daily SW speed at 1 AU and the flux expansion factor (f). From the point of view of energy transport in CHs, Fisk, Schwadron, and Zurbuchen (1999) suggested a relationship between the photospheric magnetic field strength and the SW speed. Following Wang and Sheeley (1990) and Fisk, Schwadron, and Zurbuchen (1999), Fujiki et al. (2005) investigated the relation between the SW speed and the CH properties, that is, the inverse flux expansion factor $1/f$ and the photospheric magnetic field strength B. They calculated f by taking the ratio between areas of the magnetic flux tube at the photosphere and at the source surface (SS) normalized by the distance from the Sun center:

$$f = (A_{\rm SS} \,/\, A_{\rm p})(R_{\rm S} \,/\, R_{\rm SS})^2, \quad (1)$$

where $A_{\rm SS}$ and $A_{\rm P}$ are the areas of the flux tube at the source surface and photosphere, respectively. In Fujiki et al. (2005) $A_{\rm SS}$ and $A_{\rm P}$ were estimated from the coronal magnetic field extrapolated from the photospheric magnetic field (Hakamada & Kojima 1999) and the He I 10830 Å image. $R_{\rm S}$ and $R_{\rm SS}$ are the solar radius and the radius of the SS (2.5 $R_{\rm S}$), respectively. They found a better correlation between the SW speed and the combined ratio B/f, yielding a correlation coefficient of 0.89.

Because the MEs and EUV CHs are signatures of open field lines at different layers of the solar atmosphere, we used the ratio between the areas of the ME and the EUV CH as a proxy of f. We calculated f from equation (1), where $A_{\rm P}$ and $A_{\rm SS}$ were replaced by the ME area ($A_{\rm M}$) and the EIT CH area ($A_{\rm E}$), respectively. Since ME corresponds to the chromospheric signatures (Gopalswamy et al. 1999; Moran et al. 2001), $R_{\rm S}$ and $R_{\rm SS}$ are regarded as the solar radius of the chromosphere ($R_{\rm chromosphere}$) and the lower corona ($R_{\rm corona}$). Therefore, we assumed that $R_{\rm chromosphere}/R_{\rm corona} \approx 1$. In reality, the ratio

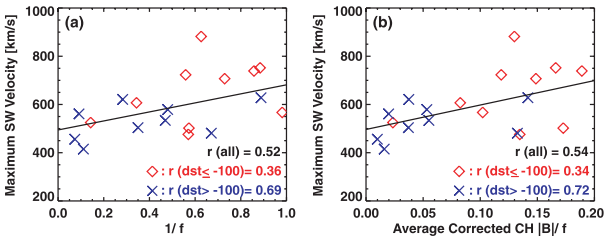

Fig. 9. Maximum solar wind speed as a function of (a) the inverse expansion factor, $1/f$, and (b) the combined parameter of $B_{\rm CH}/f$. Factor f is calculated from equation (1), where $A_{\rm P}$ and $A_{\rm SS}$ are replaced by the radio enhancement area ($A_{\rm ME}$) and the EIT CH area ($A_{\rm CH}$), respectively.

between $R_{\rm S}$ and $R_{\rm SS}$ can be as small as 0.4 (1 $R_{\rm S}$/2.5 $R_{\rm S}$). On the other hand, the area ratios may be underestimated because the coronal hole area at the SS is expected to be larger than the EUV area used here. The derived f is accurate only when the EUV CHs and the MEs are formed by an identical open-field flux tube. As we see in figure 2, the shapes of the MEs and the EUV CHs are different. It is difficult to find out how the ME area maps into the EUV area. Therefore, we should consider the derived f as being a rough proxy of the expansion factor. Although the true value of f may be different from what we derived here, we expect that they are proportional because we used the same method for all of the CHs, and hence any trend derived from the crude f may still give some useful information. Figure 9a shows a scatter plot between the inverse expansion factor, $1/f$, and the maximum SW speed. Though the correlation does not match the importance shown in figures 5a and 5b, we can see a moderate correlation in figure 9a ($r = 0.52$). The SW speed is faster when the expansion factor is smaller, i.e., for a given EUV CH area, CHs with larger MEs tend to be associated with a faster SW.

Figure 5 shows that the maximum SW speed does not have a significant correlation with the corrected absolute magnetic field strength ($B_{\rm CH}$) inside the EUV CHs and MEs. Here, we plot the maximum SW speed as a function of the combined value, $B_{\rm CH}/f$, in figure 9b. We used the magnetic field strength at the photosphere as that at the chromosphere, because the magnetic field strength does not change significantly between the two layers. Compared with figure 5e, figure 9b demonstrates that the combination of the flux expansion rate and the magnetic field strength is actually proportional to the SW speed. However, since the correlation coefficient ($r = 0.54$) is almost the same as for the flux expansion rate ($1/f$) in figure 9a, the magnetic field strength may not have a large influence on the SW speed relative to the effect of the flux expansion rate. This differs from the results by Fujiki et al. (2005), who found that the SW speed has a good correlation with B/f ($r = 0.89$), rather than with only $1/f$ ($r = 0.56$). Therefore, the moderate correlation in figure 9b might be due to the non-identical flux tube between CH and ME or the unreasonable correction of the magnetic field strength.

5. Conclusions

We investigated the relationship of the SW speed not only with EUV CH areas, but also with the chromospheric ME. Our results show that the MEs are also one of the indicators of the SW speed in the interplanetary medium. In particular, the CH area overlapping with ME area may be more important than the whole EUV CH area. Moreover, the ME area to EUV CH area ratio relates to the intensity of the geomagnetic storm. That is to say, the CHs associated with a large $A_{\rm ME}$ to $A_{\rm CH}$ ratio tend to produce large geomagnetic storms. Using the CH and ME areas, we calculated the magnetic flux tube expansion ratio, f. We examined how the maximum SW speed, V, is related to $1/f$, the corrected absolute photospheric magnetic field strength, $B_{\rm CH}$, and the combined factor, $B_{\rm CH}/f$. We found a good correlation between $1/f$ and V and the $B_{\rm CH}/f$–V, whereas the $B_{\rm CH}$–V relation is not clear.

This work was supported by NASA SR&T and LWS TR&T programs. SOHO is a project of international cooperation between ESA and NASA. This effort was supported by a NASA grant (NNM06AA33G). We thank the organizers of the "Living With a Star" CDAW meeting and the members of Working Group 1 for their event identifications. We also thank the ACE and WIND teams for the solar wind and the interplanetary magnetic field data. We further thank Dr M. Shimojo (NAOJ) for a discussion on the NoRH radio images.

References

Andretta, V., & Jones, H. P. 1997, ApJ, 489, 375
Balogh., A. J., et al. 1999, Space Sci. Rev., 89, 141
Belcher, J. W., & Davis, L., Jr. 1971, J. Geophys. Res., 76, 3534
Belenko, I. A. 2001, Sol. Phys., 199. 23
Burlaga, L. F., & Lepping, R. P. 1977, Planet. Space Sci., 25, 1151
Chertok, I. M., Grechnev, V. V., Belov, A. V., & Abunin, A. A. 2013, Sol. Phys., 282, 175
de Toma, G., & Arge, C. N. 2005, ASP Conf. Ser., 346, 251
Del Zanna, G., & Bromage, B. J. I. 1999, J. Geophys. Res., 104, A5, 9753
Fisk, L. A., Schwadron, N. A., & Zurbuchen, T. H. 1999, J. Geophys. Res., 104, A9, 19765
Fox, P., McIntosh, P., & Wilson, P. R. 1998, Sol. Phys., 177, 375
Fujiki, K., Hirano, M., Kojima, M., Tokumaru, M., Baba, D., Yamashita, M., & Hakamada, K. 2005, Adv. Space Res., 35, 2185
Gibson, S. E., et al. 1999, ApJ, 520, 871
Gopalswamy, N. 2008, J. Atomos. Sol.-Terr. Phys., 70, 2078
Gopalswamy, N., Mäkelä, P., Xie, H., Akiyama, S., & Yashiro, S. 2009, J. Geophys. Res., 114, A00A22
Gopalswamy, N., Shibasaki, K., DeForest, C. E., Bromage, B. J. I., & Del Zanna, G. 1998, ASP Conf. Ser., 140, 363
Gopalswamy, N., Shibasaki, K., & Salem, M. 2000, J. Astrophys. Astr., 21, 413
Gopalswamy, N., Shibasaki, K., Thompson, B. J., Gurman, J., & DeForest, C. 1999, J. Geophys. Res., 104, 9767
Gopalswamy, N., Yashiro, S., & Akiyama, S. 2007, J. Geophys. Res., 112, A06112
Gosling, J. T. 1996, ARA&A, 34, 35
Hakamada, M., & Kojima, M. 1999, Sol. Phys., 187, 115
Harvey, J. W., & Sheeley, N. R., Jr. 1977, Sol. Phys., 54, 343

Harvey, K. L., Sheeley, N. R., Jr., & Harvey, J. W. 1982, Sol. Phys., 79, 149
Huber, M. C. E., Foukal, P. V., Noyes, R. W., Reeves, E. M., Schmahl, E. J., Timothy, J. G., Vernazza, J. E., & Withbore, G. L. 1974, ApJ, 194, L115
Jian, L., Russell, C. T., Luhmann, J. G., & Skoug, R. M. 2006, Sol. Phys., 239, 337
Kahler, S. W., Davis, J. M., & Harvey, J. W. 1983, Sol. Phys., 87, 47
Kosugi, T., Ishiguro, M., & Shibasaki, K. 1986, PASJ, 38, 1
Krieger, A. S., Timothy, A. F., & Roelof, E. C. 1973, Sol. Phys., 29, 505
Kundu, M., & McCullough, T. 1972, Sol. Phys., 24, 133
Levine, R. H., Altschuler, M. D., & Harvey, J. W. 1977, J. Geophys. Res., 82, 1061
Luo, B., Zhong, Q., Liu, S., & Gong, J. 2008, Sol. Phys., 250, 159
Moran, T., Gopalswamy, N., Dammasch, I. E., & Wilhelm, K. 2001, A&A, 378, 1037
Munro, R. H., & Withbroe, G. L. 1972, ApJ, 176, 511
Nolte, J. T., et al. 1976, Sol. Phys., 46, 303
Obridko, V. N., Shelting, B. D., Livshits, I. M., & Asgarov, A. B. 2009, Sol. Phys., 260, 191
Ohmi, T., Kojima, M, Tokumaru, M., Fujiki, K., & Hakamada, K. 2004, Adv. Space Res., 33, 689
Parker, E. N. 1991, ApJ, 372, 719
Richardson, J. G., et al. 2006, J. Geophys. Res., 111, A07S09
Tsurutani, B. T., et al. 2006, J. Geophys. Res., 111, A07S01
Tsurutani, B. T., & Gonzalez, W. D. 1987, Planet. Space Sci., 35, 405
Tsurutani, B. T., Ho, C. M., Araballo, J. K., Goldstein, B. E., & Balogh, A. 1995, Geophys. Res. Lett., 22, 3397
Verbanac, G., Vršnak, B., Veronig, A. M., & Temmer, M. 2011, A&A, 526, A20
Vršnak, B., Temmer, M., & Veronig, A. M. 2007a, Sol. Phys., 240, 315
Vršnak, B., Temmer, M., & Veronig, A. M. 2007b, Sol. Phys., 240, 331
Waldmeier, M. 1981, Sol. Phys., 70, 251
Wang, Y.-M., & Sheeley, N. R. 1990, ApJ, 355, 726
Yashiro, S., Gopalswamy, N., Michalek, G., St. Cyr, O. C., Plunkett, S. P., Rich, N. B., & Howard, R. A. 2004, J. Geophys. Res., 109, A07105
Zhang, J., et al. 2007, J. Geophys. Res., 112, A10102
Zirker, J. B. 1977, Rev. Geophys. Space Sci., 15, 257